Heliyon 9 (2023) e14752

Contents lists available at ScienceDirect

Heliyon

journal homepage: www.cell.com/heliyon

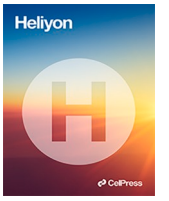

Research article

The effect of pin thread on material flow and mechanical properties in friction stir welding of AA6068 and pure copper

Majid Elyasi [a], Javad Taherian [b], Morteza Hosseinzadeh [c], Andrzej Kubit [d,*], Hamed Aghajani Derazkola [e,**]

[a] Department of Mechanical Engineering, Noushiravani University of Technology, Babol, Iran
[b] Department of Mechanical Engineering, Islamic Azad University of Sari Branch, Sari, Iran
[c] Department of Mechanical Engineering, Islamic Azad University of Ayatollah Amoli Branch, Amol, Iran
[d] Department of Manufacturing and Production Engineering, Rzeszow University of Technology, al. Powst. Warszawy 8, 35-959, Rzeszów, Poland
[e] Department of Mechanics, Design and Industrial Management, University of Deusto, Avda Universidades 24, 48007, Bilbao, Spain

ARTICLE INFO

Keywords:
Dissimilar friction sir welding
CFD simulation
Pin thread
AA6068 aluminium alloy
Copper

ABSTRACT

This study investigated the effects of friction stir welding thread on the quality of dissimilar joints between AA6068 aluminum alloy and copper. The developed computational fluid dynamic (CFD) method was employed to simulate the tool's heat generation and thermo-mechanical action. The materials flow, microstructure, mechanical properties, and hardness of joints were assessed. The results indicated that the threaded pin increased heat generation during welding. The maximum temperature recorded on the aluminum side was 780 K for the cylindrical joint and 820 K for the threaded pin joint. The size of the stir zone in the threaded pin joint was bigger than the cylindrical pin. On the other hand, mechanical interlocking between AA6068 aluminum alloy and copper increased in the threaded pin joint. The material's velocity and strain rate increased by the higher stirring action of the threaded tool. Higher strain rate and materials velocity decreased microstructure size in the stir zone. The experimental result shows that the ultimate tensile strength of the cylindrical pin joint was 272 MPa, and the threaded pin joint was 345 MPa. The average microhardness of the cylindrical pin joint was near 104 H V, and for the threaded pin was 109 H V. The results show that the ultimate tensile strength and hardness of threaded pin joint increases by 25% and 5% in comparing cylindrical pin joint.

1. Introduction

Joining and welding of dissimilar materials is an exciting and challenging field in many industrial sectors [1]. The goal commonly is to achieve a combination of both alloys' physical and thermal properties [2]. The welding of dissimilar alloys is very challenging and even impossible using conventional fusion welding techniques due to the fusion process, significant change in the structure of the material, residual stress, and intermetallic compounds that make the welding nugget brittle and result in a low-strength [3]. Solid-state welding is an excellent solution to weld dissimilar alloys because the welding is carried out at a temperature below the melting point [4]. There is no oxidation or need for protective gas, inactive environment, or consumable material. The number of defects is much less

* Corresponding author.
** Corresponding author.
E-mail addresses: akubit@prz.edu.pl (A. Kubit), h.aghajani@deusto.es (H.A. Derazkola).

https://doi.org/10.1016/j.heliyon.2023.e14752
Received 16 November 2022; Received in revised form 10 March 2023; Accepted 16 March 2023
Available online 23 March 2023

than in fusion welding [5,6]. In these processes, the heat-affected zone considered the origin of most defects and the leading cause of the drop in mechanical properties, is minimal [4]. Friction stir welding (FSW) is categorized as solid-state welding technique that was introduced by The Welding Institute (TWI) in 1991 [7]. The process was invented mainly to weld aluminum alloys [8]. The joining occurs due to frictional heat generation between the raw materials and a non-consumable tool resistant to wear and heat [9]. The plates are clamped on a semi-thick plate called the backplate to prevent movement during the welding process [10]. Then, the rotary tool penetrates the interface of the plates till the shoulder touches the surfaces of the plates. The transverse moving of the tool starts once the friction generates enough heat [11]. The FSW process produces various structures in the automobile, offshore, aerospace, and railway industries.

Nowadays, substantial research is carried out on this process to investigate the effects of different input parameters on the welding zone characteristics when of welding dissimilar alloys, such as aluminum alloys, to the copper joint [12]. Li et al. [13] concluded that intermetallic compounds affect the joint negatively. These compounds increase when the thickness increases and decrease when the thickness decreases [14]. The cooling rate is higher in thin welding sheets that restrict the diffusion time and fewer intermetallic compounds (IMCs).

Liu et al. [15] examined the layered structure in welding A506 and copper. They reported that generated frictional heat is low for the recrystallization of copper. This phenomenon leads to a layered structure instead of a metallurgic bond between two alloys. Galvão et al. [16] investigated the effects of the tool geometry on the formation and distribution of brittle intermetallic phases in friction stir welding of thin aluminum and copper sheets with a thickness of 1 mm. They concluded that the tool geometry has a significant role in forming and distributing IMCs [17]. Xue et al. [18] reported that the formation of harmful intermetallic layers could be avoided by a proper tool offset on the aluminum side, lower tool rotational speed, and bigger tool shoulder diameter. Saeid et al. [19] investigated the weldability of pure aluminum and copper by friction stir welding. They reported that defects such as voids and cracks are generally present when pure aluminum is welded to copper. Intermetallic compounds, including Cu_9Al_4, CuAl, and $CuAl_2$, are the most common ones that deteriorate joint strength due to their brittleness. Tan et al. [20] and Xue et al. [21] demonstrated that the structure of intermetallic compounds affects the mechanical properties of the joint significantly. Although a thin layer of Al–Cu intermetallic compound promotes the joint's mechanical properties, a thick IMC layer significantly deteriorates the joint strength [22]. The available literature shows that many aspects of dissimilar joints between aluminum alloys and copper are not fully understood. Due to the complexity of the FSW process, the simulation approach helps better understand thermo-mechanical phenomena during joining.

The literature on the simulation of dissimilar FSW joints between aluminum alloy and copper is limited. Aalami-Aleagha et al. [23] simulated the FSW joint between 1050-H16 aluminum alloy and copper using the computational fluid dynamic (CFD) method. They examined the FSW tool offset effects on the joint's heat generation and temperature gradient. Sun et al. [24] used CFD methods to simulate 6061 aluminum alloy and copper dissimilar FSW joints. Their study used a pinless tool to determine fluid flow and heat generation. Kadian and Biswas [25] simulated the FSW joint of AA6061 aluminum alloy and Cu–B370 with the volume of fluid (VOF) approach. They showed that the heat flux was unsymmetrical due to the different thermal properties of base metals. Iordache et al. [26] employed coupled Eulerian-Lagrangian (CEL) to analyze the influence of rotational tool speed on the temperature distribution of

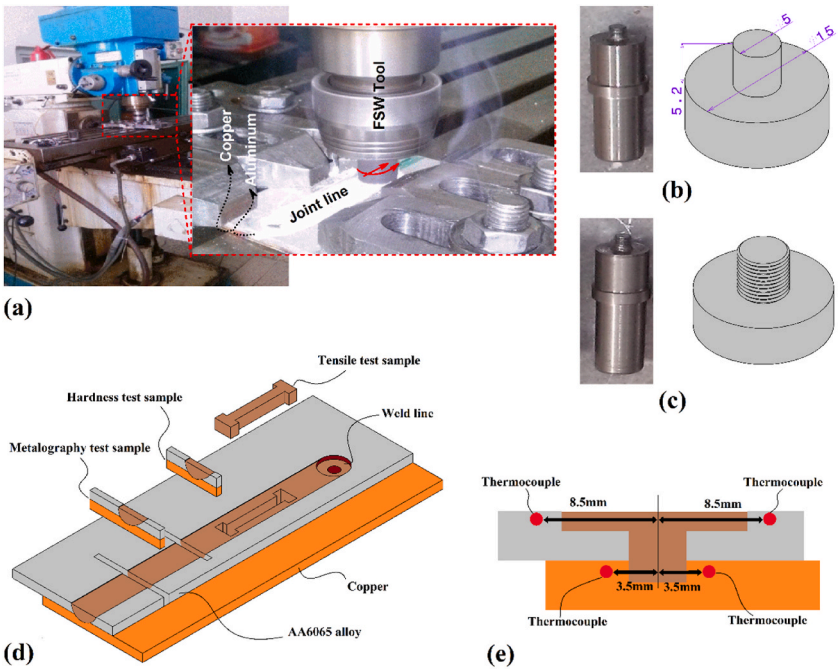

Fig. 1. (a) Friction Stir Welding of aluminum-copper, (b) welding tools with (b) a cylindrical, and (c) a threaded pin. (d) Schematic illustration of the welded sample and cutting direction of tensile test, metallography, and hardness tests. (e) Schematic illustration of thermocouples placements.

the FSW of AA1200 aluminum alloy and copper. They stated that placing base metal on the advancing side (AS) or retreating side (RS) changes the total heat generation. They showed that the total heat increased when the aluminum alloy was placed in AS. Patel et al. [27] used the CLE approach to simulate cooling-assisted FSW of aluminum to the copper joint. The heat loss was assumed as convective heat transfer for the cooling procedure. Naqibi et al. [28] used the CLE method to perform a thermal analysis of AA5086 aluminum alloy and Cu12200 pipe. They used various tools, rotational speed, and traveling speed to find the ideal heat input to obtain the maximum joint tensile strength. They stated that the maximum heat generation due to plastic deformation during this joint was 13% of the total generated heat.

On the other hand, AA6068 aluminum alloy has high tensile strength and resistance to corrosion. Due to uniform crystals, pure copper (Cu) has good hardness, formability, heat transfer coefficient, and corrosion resistance. Thus, the welding of these alloys could apply in industries such as shipbuilding, electrical industries, automotive, optic, heat exchangers, boilers, heaters, and coolers. The present paper investigates the effect of pin thread on mechanical properties and material flow in the FSW of AA6068-Copper dissimilar joint. According to the available literature, there is no report on the investigation of the effect of the pin thread on heat generation, mechanical properties, and material flow of aluminum-copper joints [29]. The effect of thread pins on the amount of heat on the aluminum and copper sides can give precise information about the welding quality in joint lap configuration.

2. Materials and methods

The 3 mm thick sheets of AA6065 aluminum alloy and copper were selected for experimental tests. A modified universal milling machine was used as an FSW machine for the welding procedure. The sheet surfaces were polished and cleaned before welding. The aluminum sheet was the upper sheet in the welding clamp, and the copper sheet was the lower one, which is presented in Fig. 1a. The mechanical properties of AA6065 aluminum alloy and copper were tested in the laboratory. The obtained mechanical properties of base metals results are presented in Table 1. The tensile and shear properties of raw materials and welded samples proceeds according to the ASTM E8 and ASTM E384 standards, respectively. The thermal properties of raw materials were evaluated according to ASTM C177.

Two types of FSW tools with cylindrical and threaded pins were selected to evaluate their effects on the properties of the final joint. Both tools had a 15 mm shoulder diameter with a 3° concave and a 5 mm pin diameter with a 5.2 mm length. All tools were made of H13 tool steel. The cylindrical pin surface was smooth, and the other pin was manufactured with an M5 thread shape. Pictures of cylindrical and threaded pins are presented in Fig. 1b and c, respectively. The tool rotation direction was counter-clockwise, and a tilt angle of 3° was used. The rotational tool speed was 1130 rpm, and the transverse speed was 24 mm/min. For evaluation of the mechanical properties of the final joint, tensile test specimens were prepared parallel to the welding line according to the ASTM/E8-M03 using the WEDM machine for each experiment set. The tensile test is repeated three times, and average results are reported. A metallography sample and hardness test were implemented to find pin threat's effects on the final joint's metallurgical properties. Four K-type thermocouples were selected for measuring thermal changes during the process; two were placed on the aluminum side, and others were placed on the copper side. The thermocouples joint to raw materials with Capacitor Discharge Welding (CD Welding) process. A schematic view of mechanical testing samples and placement and position of thermocouples are depicted in Fig. 1d and e, respectively.

3. Process modelling

3.1. Governing equation

The friction stir welding process of AA6068 aluminum alloy and copper was simulated by the computational fluid dynamic (CFD) technique and volume of fluid (VOF) approach. The mass, momentum, and energy equations were considered during the process simulation by the CFD technique. The volume fraction of phase k is considered by Ω_k for describing phase distribution. The mass conservation equations are derived as [30]:

$$\underset{\sim}{\nabla}.\left(\Omega_k \rho_k \underset{\sim}{u}\right) = \sum_{j=1}^{2}\left(\dot{m}_{jk} - \dot{m}_{kj}\right) \tag{1}$$

In Equation (1), the mass transfer rate from phase k to phase j is present as $\dot{m}_{kj}$ and shifted condition defined by $\dot{m}_{jk}$ which involved AA6068 alloy and cooper. The equation of momentum conservation in the 3D can be defined by Ref. [31]:

$$\underset{\sim}{\nabla}.\left(S\underset{\sim}{\underset{\sim}{u}}\right) = -\underset{\sim}{\nabla}P + \underset{\sim}{\nabla}.\Psi \tag{2}$$

Table 1
Properties of AA6068 aluminum alloy and cooper.

Alloy	Tensile Strength (MPa)	Yield Strength (MPa)	Shear Strength (MPa)	Elongation (%)	Hardness (Vickers)	Thermal conductivity W/m.K
AA6068	460	300	205	10	91	180
Cu	392	236	235	12	104	398

In Equation (2), the S is the average material density by volume fraction that can be presented by Equation (3) [31]:

$$S = \sum_{k=1}^{2} \Omega_k \rho_k \tag{3}$$

In Equation (2), Ψ is the shear stress tensor which defines as Equation (4) [32]:

$$\Psi = \overline{\mu}\left(\underset{\sim}{\nabla} \otimes \underset{\sim}{u} + \underset{\sim}{\nabla} \otimes \underset{\sim}{u}^{T}\right) \tag{4}$$

Which in Equation (5):

$$\overline{\mu} = \sum_{k=1}^{2} \Omega_k \mu_k \tag{5}$$

Finally, the Equation of energy is presented by Equation (6) [33]:

$$\underset{\sim}{\nabla}.\left[\left(\sum \Omega_k \rho_k ck\right) T\underset{\sim}{u}\right] = -\underset{\sim}{\nabla}.\underset{\sim}{q} + \underset{\sim}{\nabla}.\left[\left(\Psi - p\underset{\sim}{I}\right).\underset{\sim}{u}\right] \tag{6}$$

T is temperature, the specific heat capacity of the phase k is defined by c_k. $\underset{\sim}{q}$ is heat flux that presents by temperature gradient and average thermal conductivity in Equation (7):

$$\underset{\sim}{q} = \overline{K}\nabla T \tag{7}$$

Where in Equation (8):

$$\overline{K} = \sum_{k=1}^{2} \Omega_k K_k \tag{8}$$

that K_k is the thermal conductivity of each phase.

4. Materials model

In this section detail of material behaviours are discussed. In Equation (5), μ_k is refer to the non-Newtonian viscosity of each base material that can be determined as follows as Equation (9) [34]:

$$\mu_k = \frac{\sigma_e}{3\dot{\varepsilon}} \tag{9}$$

$\dot{\varepsilon}$ indicated strain rate and σ_e is flow stress proposed by Equation (10) [35]:

$$\sigma_e = \frac{1}{\alpha} arc\sinh\left(\frac{Z}{A}\right)^{\frac{1}{n}} \tag{10}$$

where A, a, and n are material constants for raw material. The Z is defined as Zener–Hollomon parameter in Equation (10) and presented in Equation (11):

$$Z = \dot{\varepsilon} exp^{\left(\frac{Q}{RT}\right)} \tag{11}$$

In Equation (11), the Q represents the activation energy, and the amount of Q is 158.3 kJ/mol; R represents the universal gas constant, $\dot{\varepsilon}$ which signifies the effective strain rate. The effective strain rate is given by Equation (12):

$$\dot{\varepsilon} = \sqrt{\left(\frac{2}{3}\varepsilon_{ij}\varepsilon_{ij}\right)} \tag{12}$$

In Equation (12), the ε_{ij} represents the strain rate tensor and defined by Equation (13):

$$\varepsilon_{ij} = \frac{1}{2}\left(\frac{\partial u_i}{\partial x_j} + \frac{\partial u_j}{\partial x_i}\right) \tag{13}$$

5. Boundary conditions

The generated heat during FSW process (Q_t) consists of generated heat by friction (Q_i) and generated heat by plastic deformation (Q_b) [36].

$$Q_t = Q_i + Q_b \tag{14}$$

In Equation (14), the heat generated by friction at the interfaces of tool and base metals can be defined by Equation (15):

$$Q_i = \left[(1-\delta)\eta\tau + \delta\mu_f P_N\right](\omega r - U_1 \sin\theta) \tag{15}$$

In Equation (15), the Q_b is generated heat rate per unit volume that is the result of plastic deformation outside area in the interface of workpieces and tools which is defined as Equation (16):

$$Q_b = \frac{d\dot{\varepsilon}_p}{dV} = \beta\mu\varphi \tag{16}$$

that φ is given by Equation (17):

$$\varphi = 2\sum_{i=1}^{3}\left(\frac{\partial u_i}{\partial x_i}\right)^2 + \left(\frac{\partial u_1}{\partial x_2} + \frac{\partial u_2}{\partial x_1}\right)^2 + \left(\frac{\partial u_1}{\partial x_3} + \frac{\partial u_3}{\partial x_1}\right)^2 + \left(\frac{\partial u_3}{\partial x_2} + \frac{\partial u_2}{\partial x_3}\right)^2 \tag{17}$$

The value of β is a range between 0 and 1. The value of 1 is selected for a well-mixed system on a molecular scale, and 0 is for a non-mixing case. The mass conservation equation for each workpiece in low concentration is expressed as Equation (18) [37]:

$$\frac{\partial(u_j C_i)}{\partial x_j} = -V\frac{\partial C_i}{\partial x_1} + \frac{\partial}{\partial x_1}\left(D\frac{\partial C_i}{\partial x_j}\right) \tag{18}$$

The V is the vertical speed of plastic material, and the expression of D refers to the temperature-dependent chemical diffusion, which is defined as Equation (19) [38]:

$$D = A_1 e^{\left(\frac{Q_1}{RT}\right)} + A_2 e^{\left(\frac{Q_2}{RT}\right)} \tag{19}$$

6. Heat transfer model

In the friction stir welding process, a part of generated heat is transferred to the tool. For this reason, amount of heat that conducted to the tool can be defined by a coefficient as Equation (20):

$$\gamma = \frac{\left(\sqrt{k\rho C_p}\right)_{workpiece}}{\left(\sqrt{k\rho C_p}\right)_{tool} + \left(\sqrt{k\rho C_p}\right)_{workpiece}} \tag{20}$$

Then the total heat can be defined by Equation (21):

$$Q_T = \gamma Q_t \tag{21}$$

In this study, the configuration of the weld was a lap joint. It means the aluminum alloy is placed at the top and the copper sheet at the bottom. The back side of the copper sheet was in contact with the fixture, and the sides were in touch with the air. On the other hand, the aluminum plate's back side was connected with the copper sheet's upside, and other parts of the aluminum alloy were in contact with air. Accordingly, the heat transfer of base metals with the surrounding environment is not the same. Due to raw metal contact, various types of heat transfer models were selected. At the bottom surface, conductive heat transfer between the cooper backing plate and fixture was considered that presented in Equation (22):

$$k\left.\frac{\partial T}{\partial Z}\right|_{Bottom} = h_b(T - T_a) \tag{22}$$

The heat transfer coefficient at the bottom face depended on the local temperature through the following Equation (23):

$$h_b = h_{b0}(T - T_a)^{0.25} \tag{23}$$

As mentioned earlier, the aluminum alloy's joint line and top surface were in direct contact with air. For this reason, convective and radiation heat transfer models were assumed for those areas as Equation (24):

$$-k\left.\frac{\partial T}{\partial Z}\right|_{Top} = \mathrm{B}\varepsilon\left(T^4 - T_a^4\right) + h_t(T - T_a) \tag{24}$$

In Equation (24), h_t is the convective heat transfer coefficient at the top surface. The welding domain consists of aluminium alloy and

copper as weldments. All weldments were meshed by Tetrahedral/Hybrid elements. The meshes had a T-grid combination shape. The area near the pin tool and heat source was meshed by finer mesh. This approach was selected for more accurate heat transfer and material flow evaluation. To optimize simulation time, a sizing function was used to increase the mesh size far from the heat source. In this case, the heat and mass flow can be monitored easily in a total of 1,454,200 vol of meshes created for all simulation domains. A view of the meshed model is shown in Fig. 2.

7. Results and discussion

7.1. Thermal history

The thermal history of the FSW process is a significant factor in analyzing final product quality. Table 2 presents the experimental and simulation results of welding between AA6068 aluminum alloy and copper. The results are shown the recorded temperature in AS and RS. The experimental results show the maximum temperature produced in the AA6068 aluminum alloy in both samples. Due to obtained results, the heat generation in the sample with a threaded pin was more than a cylindrical pin. Due to the placement of raw materials, the AA6068 aluminum alloy was on top, and the FSW tool shoulder had straight contact with the AA6068 aluminum alloy. Due to the experimental results, the maximum recorded heat in the joint welded by a cylindrical pin was 780 K, while the maximum recorded heat in the joint welded by a threaded pin was 820 K. On the other hand, the maximum heat predicted by simulation in the cylindrical pin and the threaded pin was 796 K and 803 K, respectively. For this reason, the total heat generation in the AA6068 aluminum alloy was more than the copper side.

The simulation results of surface heat flux on the top surface of AA6068 aluminum alloy and copper at cylindrical and threaded pin cases are presented in Fig. 3a, b, 3c and 3d, respectively. The results revealed that the heat flux on AA6068 aluminum surfaces is more than on copper surfaces. More heat generation on the AA6068 aluminum side leads to more heat flux. On the other hand, the lower contact area between the tool and copper caused lower heat generation and, consequently, lower heat flux on the surface of the copper side. The simulation results revealed more heat generation in threaded pins than in the cylindrical pin. The heat concentration in AS was more than RS. The rotational direction of the tool caused the heat concentration in AS to be more than RS. This behaviour is detectable in both cases and both alloys. Due to obtained results, the maximum generated heat in the joint that was welded by a cylindrical pin was 5% lower than that of a threaded pin.

The maximum heat generation difference between the AA6068 aluminum side (780 K) and copper side (660 K) was near 200 K in a cylindrical pin joint. Meanwhile, the maximum heat generation difference between the AA6068 aluminum side (820 K) and the copper side (670 K) was near 150 K in a threaded pin. The results indicate that the temperature difference between AA6068 aluminum alloy and copper decreased with increasing heat generation in threaded pins. The total heat generation and surface heat flux directly affect the material's surface flow. Fig. 3e and 3f are presents the surface flow of specimens welded by cylindrical and threaded pins. The surface material flow contains continuous onion rings on the AA6068 aluminum sheet surface in both samples. Due to the significance of the tool shoulder in the surface material flow, there is not a noteworthy difference in surface material flow for specimens that are welded by the cylindrical pin (Fig. 3e) and the threaded pin (Fig. 3f). The only difference was the small flash formed in RS of joint line welded by Threaded pin. Also, the surface roughness of the cylindrical pin joint was more than the threaded pin joint. The joint line color is the same as the AA6068 aluminum color of the upper sheet. This indicates that copper as the lower sheet could not penetrate in upper layers and change the color of the welding line in both cases. The total heat generation and heat flux affect this joint's flash formation and joint line roughness.

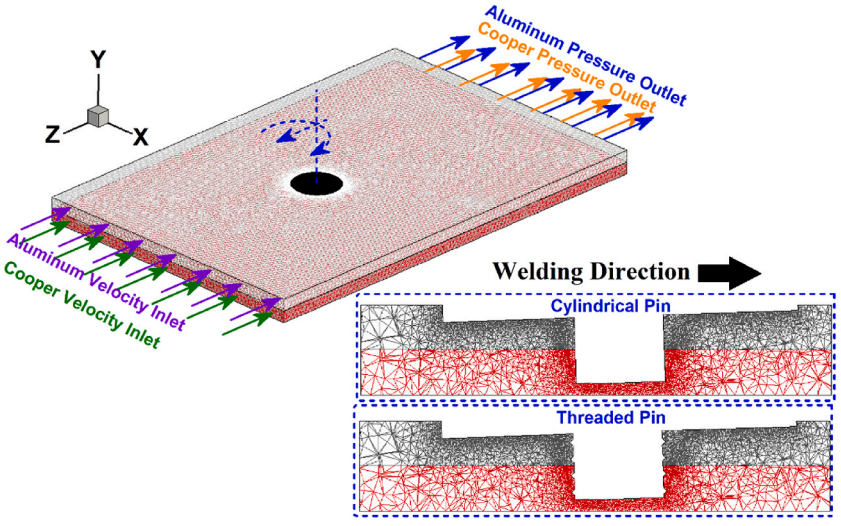

Fig. 2. Schematic view of UFSW process modelling.

Table 2
Comparison between maximum temperature that recorded and simulated.

Tool	Part	Experimental result		Simulation results	
		AS	RS	AS	RS
Cylindrical Pin	Al	780 K	777 K	769 K	766 K
	Cu	660 K	658 K	625 K	621 K
Threaded Pin	Al	820 K	818 K	803 K	799 K
	Cu	670 K	668 K	648 K	642 K

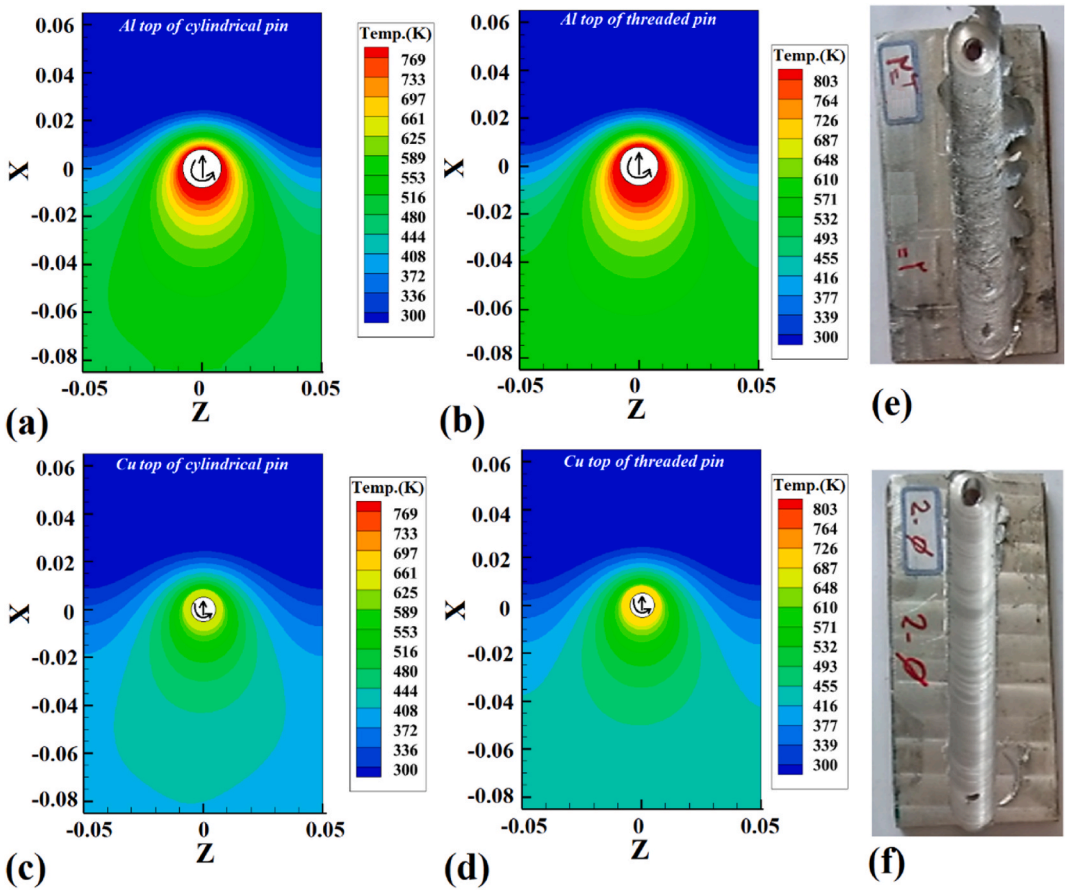

Fig. 3. Simulation result from surface heat flux on aluminum alloy at (a) cylindrical pin and (b) threaded pin samples. Simulation result from surface heat flux on aluminum alloy at (a) cylindrical pin and (b) threaded pin samples. The surface material flow of the specimen is welded by (e) the simple pin, and (f) the threaded pin.

7.2. Internal material flow

The internal heat flux, similar to surface heat flow, can show the properties of the final joint. For this reason, the internal heat flux of the FSW joints is depicted in Fig. 4a and b. The internal heat flux was similar to the surface heat flux. In both cases, the heat in the upper sheet (AA6068 aluminum alloy) was more than in the lower sheet (copper). At this point, two main factors affect the internal heat flux. First, the total amount of heat generation. As discussed before, the heat generation on the AA6068 aluminum side was more than on the copper side. The generated heat at interfaces of raw materials affects the form of interfaces in the stir zone. For this reason, the heat flux in this area is more. Second, copper's thermal conductivity is almost double that of AA6068 aluminum alloy.

For this reason, the heat flux in copper sheets is lower than in AA6068 aluminum sheets (in both cases). On the other hand, more heat generation in threaded pin cases leads to more heat flux. The simulation results of the interface of raw sheets indicated that the generation heat at the interface of raw materials in the cylindrical pin joint was 601 K, while the generated heat in the threaded pin joint case was 660 K. The cross-sections of the welded joints by cylindrical and threaded pins are presented in Fig. ca and 4 d, respectively. According to the experimental results, the internal material flow presents no void and defects at the macroscale. The

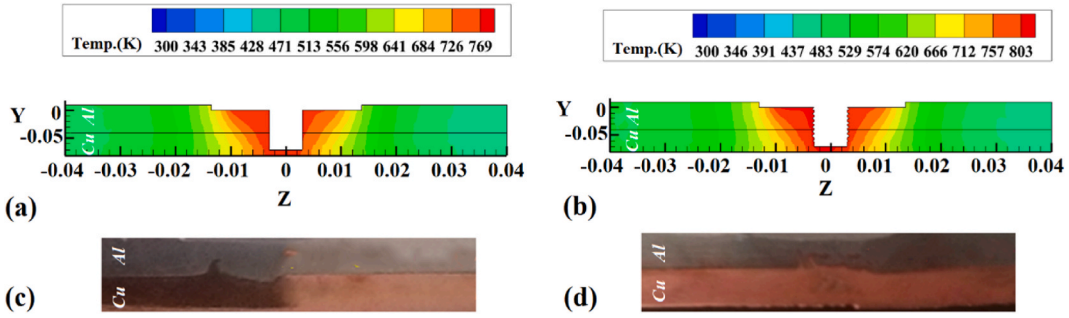

Fig. 4. Cross section views from simulation results of internal heat flux in (a) cylindrical pin and (b) threaded pin tool samples. Cross section views from FSW sample that welded with by (c) cylindrical pin and (d) threaded pin tool samples.

cross-section view of the cylindrical pin joint indicated the copper penetration in the AA6068 aluminum sheet. The interaction of copper in the AA6068 aluminum alloy was limited, which seems to be due to insufficient extrusion of copper on the AA6068 aluminum side. The stretching of copper in AA6068 aluminum alloy at the interface results from the stirring action of the pin. The joint interface that was welded with a threaded pin was different. The stretching of copper in the AA6068 aluminum sheet was intense with a wavy shape. This type of interface represents that the threaded pin increases its forging force inside the stir zone—consequently, the bonding and mechanical interlocking of copper and AA6068 aluminum alloy increases.

The cross-section of joints was analyzed with a new approach to better study internal materials flow. For this reason, a cross-section view of FSW samples with cylindrical and treaded pins is depicted in Fig. 5a and b, respectively. The experimental results indicate that the stir zone of the joint formed between AA6068 and copper. The results indicated that the stir zone is a mixture of AA6068 aluminum alloy and copper plus an interface line between two materials. The size of the stir zone at the threaded pin joint was bigger than the cylindrical pin joint. The thermo-mechanical affected zone (TMAZ) and heat-affected zone (HAZ) formed around the stir zone. Due to the high difference between the shear stress of base materials, the stir zone is not similar to the regular FSW joint. The TMAZ area is formed in AA6068 aluminum alloy and copper sides. Higher heat generation by threaded pin caused the TMAZ and HAZ areas in this sample was formed bigger than the cylindrical pin joint. The interface line is the main point in the stir zone of welded samples. The interface of the cylindrical pin sample indicated the deforming of copper and stretching in AA6068 aluminum alloy. The threaded pin's higher stirring action increased copper's stretching in AA6068 aluminum alloy. Higher heat generation and stirring action of threaded pin increased the interaction of base metals. As can be seen, the intense lamellar structure formed at the interface of base metals in the stir zone of the joint that was welded by a threaded pin.

8. Materials velocity

The simulation results of materials velocity at FSW samples with cylindrical and threaded pins are depicted in Fig. 6a and b, respectively. The results consist of a cross-section view of joints and statical analysis from materials velocity at different parts. The results indicated that the velocity of the materials in the AA6068 aluminum sheet was more than on the copper side. The material velocity in the joint line is related to the stirring action of the FSW tool.

More heat decreases the shear stress of the base material and increases the movement of hot materials by the FSW tool. This phenomenon is due to higher heat generation on the AA6068 aluminum side. On the other hand, comparing two samples indicates that

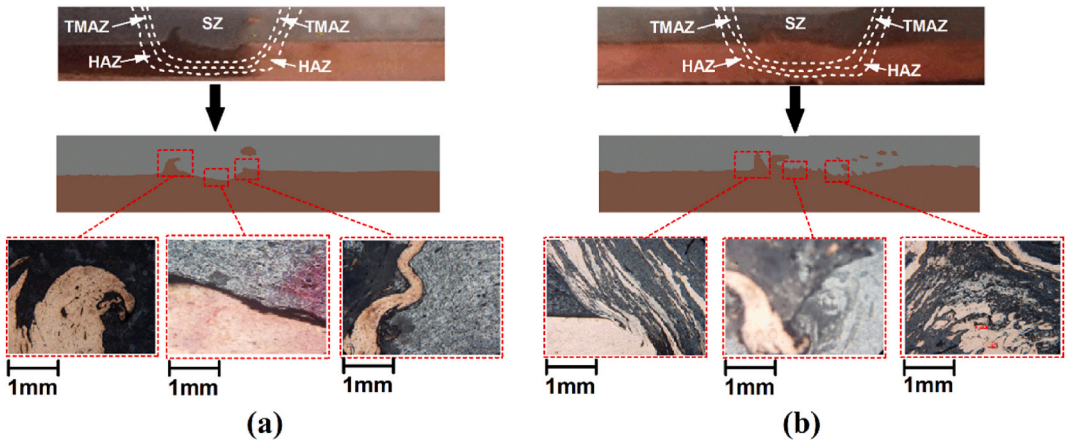

Fig. 5. Cross section views from FSW sample that welded with by (a) cylindrical pin and (b) threaded pin tool samples.

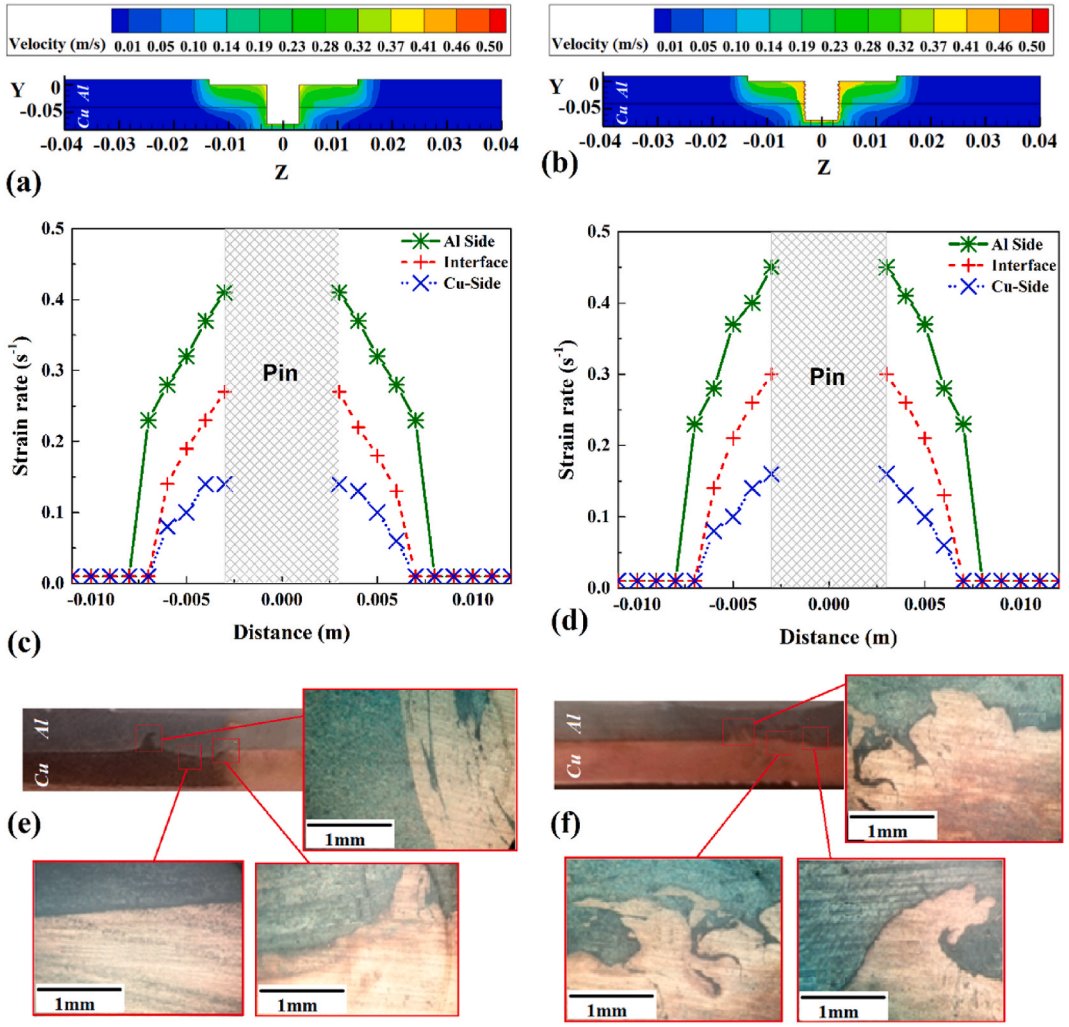

Fig. 6. Cross-section view of simulation results of materials velocity at (a) cylindrical and (b) threaded pin. Statical results of materials velocity at (c) cylindrical and (d) threaded pin. The internal material flow of the specimen that is welded by (e) the cylindrical pin and (f) the threaded pin.

the more heat generation by a threaded pin, the higher the materials' velocity. Three lines were selected inside the stir zone to understand material velocity changes better. The first line was selected below the shoulder. The second was on the interface, and the last was selected in the middle of the copper sheet. The results of cylindrical and treated samples are presented in Fig. 6c and 6d, respectively. The results indicate that the materials velocity below of tool shoulder was higher than in other areas. The maximum materials velocity in cylindrical and treaded pin joints were 0.42 m/s and 0.47 m/s, respectively. Higher heat generation in threaded pin samples increased materials velocity by 0.05 m/s. The materials velocity decreased at the interface of samples due to lower heat generation in this area. The material velocity at the cylindrical and threaded pin interface was 0.29 m/s and 0.33 m/s, respectively. The materials velocity on the copper side for the cylindrical and threaded pin was 0.13 m/s and 0.15 m/s, respectively. It should be noticed that according to the simulation results, materials velocity at the interface of raw sheets leads to bonding and mechanical interlocking. As discussed before, the higher heat generation and velocity of materials at the interface of threaded pin leads to the wavy interface. The high magnification image of FSW samples approved this point. The interface of base metals at the joint that welded with a threaded pin was wavier (Fig. 6e) than the cylindrical pin sample (Fig. 6f). This material flow results from higher material velocity that increases the interaction of hot metals in the stir zone.

9. Strain rate and microstructure of joint

The strain rate results of cylindrical and threaded pin joins are presented in Fig. 7a and b, respectively. The results indicated that the strain rate of the joint line in the threaded pin sample is more than cylindrical pin sample. Due to higher heat generation and material velocity in the threaded sample, a higher strain rate is expected. The statistical results of strain rate at various parts of the joint line (similar to materials velocity) are presented in Fig. 7c and d, respectively. The results indicated that the maximum strain rate in the

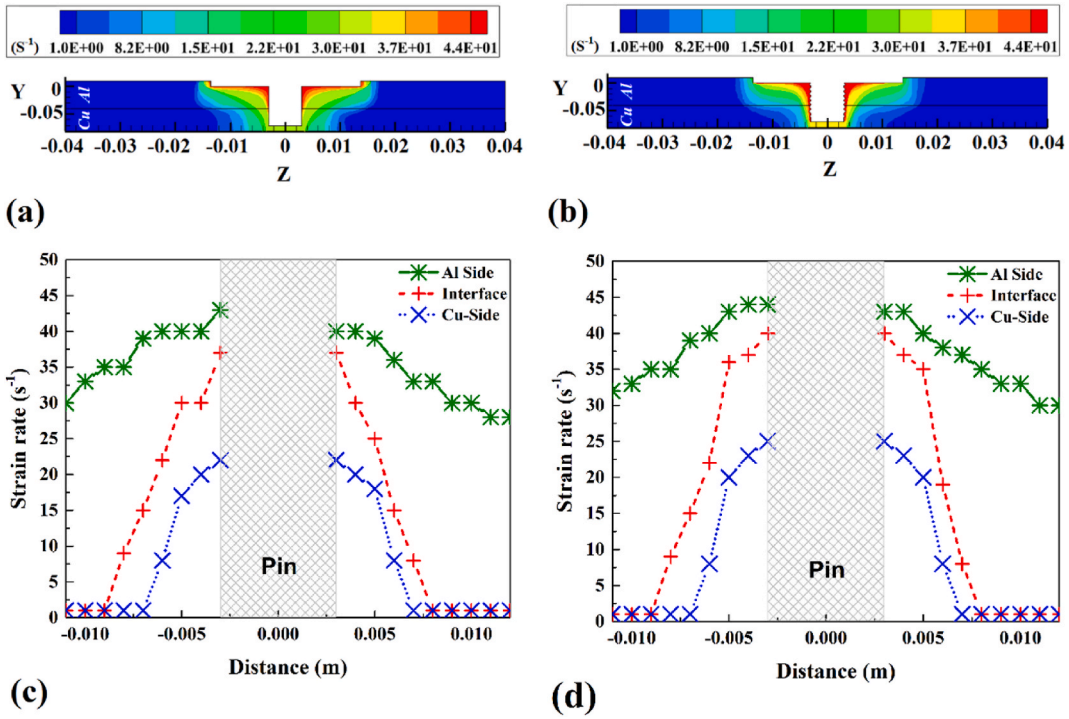

Fig. 7. Cross-section view of simulation results of materials velocity at (a) cylindrical and (b) threaded pin. Statical results of materials velocity at (c) cylindrical and (d) threaded pin.

threaded pin sample (46s^{-1}) is 5s^{-1}, more than the cylindrical pin sample (41s^{-1}).

Also, analyzing the strain rate at the interface of raw materials, the average strain rate in the threaded pin sample was 34 s^{-1}, while the average strain rate of the cylindrical pin sample was 37 s^{-1}. The higher heat generation in the threaded pin sample decreased base metals viscosity; Consequently, materials velocity and strain rate increased in this sample. The strain rate of the stir zone directly

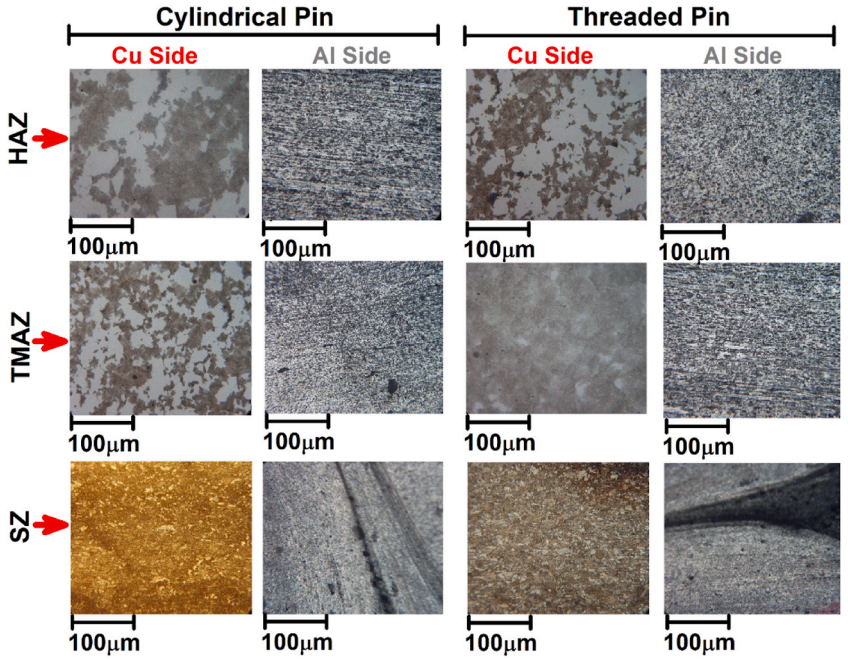

Fig. 8. Optical microscopy image from microstructure changes in different parts of FSW samples.

affects the microstructure of the final joint. The microstructure of different parts of FSW joints is presented in Fig. 8. The higher strain rate indicated more stirring (thermo-mechanical) action. The microstructure size in the stirring zone results from the tool's stirring action after welding. For a better understanding of the strain rate effect, the microstructure of the joint for both samples is analyzed. The results indicate that the grain size in threaded and cylindrical samples differs. The experimental results show that the grain size in copper and AA6068 AA6068 aluminum alloy was 15 μm and 6 μm, respectively. Small size grain in the centre of the stir zone for both samples was detected. Comparing samples in the stir zone indicated that the microstructure of AA6068 aluminum alloy and copper in threaded pin joint were smaller than in cylindrical pin tool joint.

The higher strain rate of war materials in the threaded pin tool was the reason for this phenomenon. For welded sample by the cylindrical pin, the grain size in the stir zone was 8.9 μm and 2.1 μm for copper and AA6068 aluminum, respectively. Due to more stirring action and thermo-mechanical work for the specimen welded by the threaded pin, the grain size of copper and AA6068 aluminum is 8 μm and 1.8 μm, respectively. This trend was also repeated in a thermo-mechanical affected zone (TMAZ). Higher heat generation and heat flux in the threaded pin increased the static recrystallization of base metals in the heat-affected zone (HAZ) compared to the cylindrical pin sample.

9.1. Tensile strength

The tensile test is a standard test to evaluate the mechanical properties of joints. The tensile test results of different samples are presented in Fig. 9.

According to the results, the biggest stir zone in the threaded pin sample caused higher tensile strength. Higher interaction between raw materials at the interface line in the stir zone is another reason that increased the final joint strength in the threaded pin case. The results revealed that the ultimate tensile strength of the welded joint with threaded and cylindrical pins was 345 MPa and 272 MPa, respectively (Fig. 9a). Fig. 9b and c presents the SEM image from the fracture surface of the tensile test of the threaded and cylindrical pins. The brittle fracture is evident for both specimens welded by the threaded and cylindrical pins.

9.2. Microhardness

The microhardness profile of the welded specimens by both tools is presented in Fig. 10.

According to the results, the microhardness values increase moving toward the weld centre due to more refined grains resulting from dynamic recrystallization at the stir zone. The microhardness values are bigger when the threaded pin is used. As mentioned before, the material volume displaced by the threaded pin is more than that of the cylindrical pin. More stirring by the threaded pin results in more refined grains and higher microhardness values. Due to tool rotation, more material is displaced from the retreating side to the advancing side, and more heat is generated on the advancing side. Thus, the microhardness values are higher on this side, represented by a step in the diagram. The maximum microhardness value for the welded sample was on the interface line. The results show that the hardness of the specimen welded by the threaded pin was 109 HV at the center of the stir zone, while the specimen welded by the cylindrical pin was 104 HV.

10. Conclusion

In the present research, the effects of the FSW tool pin thread on AA6068 and the copper joint were investigated. The VOF technique simulated the FSW process, and the output results are summarized as follows.

1. The internal heat generation in the threaded pin was more than in the cylindrical pin. Higher heat generation leads to more material stirring and the internal material mixing between AA6068 aluminum alloy and copper.
2. The experimental results revealed that the generated heat in the SZ of the joint welded with a threaded pin was 5% more than the cylindrical pin sample. This difference caused increasing in materials velocity by 12%. Increasing heat generation and materials velocity leads to more mechanical interlocking between raw materials.
3. Simulation results revealed that the strain rate of the stir zone from 41 s^{-1} at the cylindrical pin sample increased to 46s^{-1} in the threaded pin sample. A higher strain rate leads to a more refined microstructure. Smaller microstructure in threaded pin sample increased the hardness of joint interface by ~5% and increased the ultimate tensile strength of the joint by 12%.

Author contribution statement

Majid Elyasi; Javad Taherian; Morteza Hosseinzadeh: Performed the experiments; Analyzed and interpreted the data; Contributed reagents, materials, analysis tools or data.

Andrzej Kubit; Hamed Aghajani Derazkola: Conceived and designed the experiments; Wrote the paper.

Funding statement

This research did not receive any specific grant from funding agencies in the public, commercial, or not-for-profit sectors.

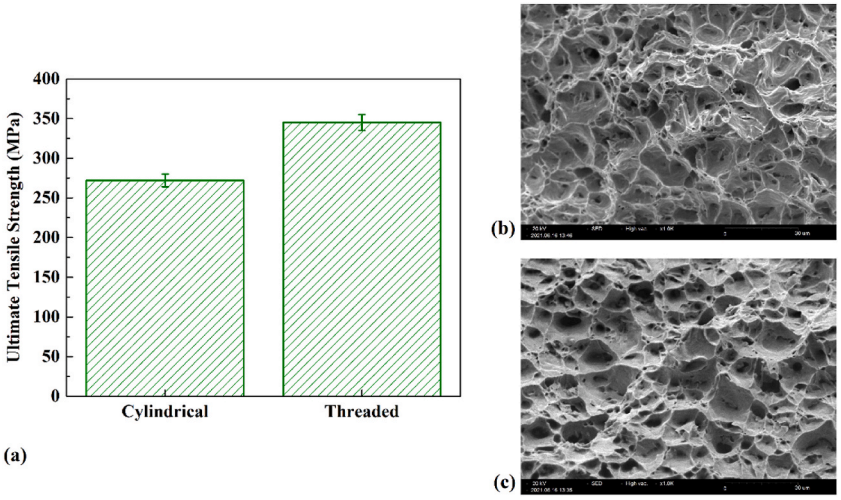

Fig. 9. (a) Ultimate tensile strength of FSW samples. ESM image of tensile test fractured sample that FSW with (b) threaded and (c) cylindrical pin.

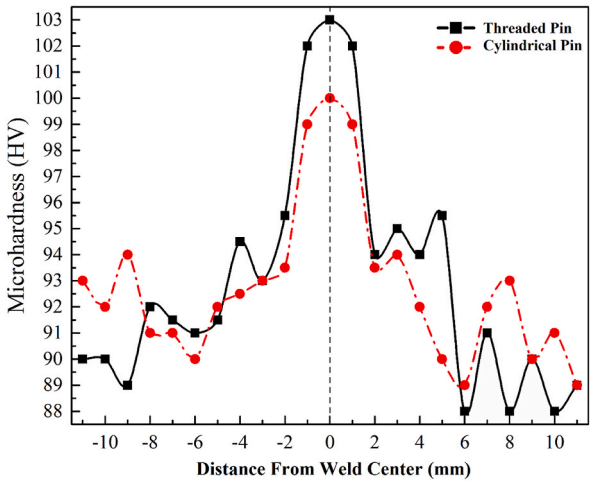

Fig. 10. The comparison of microhardness values that are welded with different tools.

Data availability statement

Data included in article/supplementary material/referenced in article.

Declaration of interest's statement

The authors declare no conflict of interest.

Nomenclature

FSW	Friction stir welding
AS	Advancing side
RS	Retreating side
SZ	Stir zone
HAZ	Heat affected zone
TMAZ	Thermo-mechanical affected zone
$\underset{\sim}{\nabla}$	special vector differential operator
ρ_k	the density of k phase

$\underset{\sim}{u}$	Velocity gradient
$\dot{m}_{kj}$	mass transfer rate from phase k to phase j
$\dot{m}_{jk}$	mass transfer rate from phase j to phase k
P	pressure field
φ	shear stress tensor
β	mixing constant at the atomic scale
T	Temperature
c_k	specific heat
K_k	Thermal conductivity
$\dot{\varepsilon}$	Strain rate
σ_e	Flow stress
ε_{ij}	Strain rate tensor
r	radial distance of the centre
τ	maximum shear stress at yielding
η	mechanical efficiency
δ	fractional slip between the tool and the workpiece interface
μ_f	coefficient of friction
P_N	axial force
V	vertical speed of plastic material
D	Temperature-dependent chemical diffusion
B	Stefan–Boltzmann constant
ε	emissivity

References

[1] S. Manickam, C. Rajendran, V. Balasubramanian, Investigation of FSSW parameters on shear fracture load of AA6061 and copper alloy joints, Heliyon 6 (2020), e04077, https://doi.org/10.1016/j.heliyon.2020.e04077.

[2] J. You, Y. Zhao, C. Dong, S. Miao, Z. Liu, L. Liu, Y. Su, Microstructural evolution and mechanical properties of the Al–Cu dissimilar joint enhanced by stationary-dynamic shoulder friction stir welding, J. Mater. Process. Technol. 300 (2022), 117402, https://doi.org/10.1016/j.jmatprotec.2021.117402.

[3] N. Gotawala, A. Shrivastava, Analysis of material distribution in dissimilar friction stir welded joints of Al 1050 and copper, J. Manuf. Process. 57 (2020) 725–736, https://doi.org/10.1016/j.jmapro.2020.07.043.

[4] J. Victor Christy, A.H. Ismail Mourad, M.M. Sherif, B. Shivamurthy, Review of recent trends in friction stir welding process of aluminum alloys and aluminum metal matrix composites, Trans. Nonferrous Met. Soc. China (English Ed. 31 (2021) 3281–3309, https://doi.org/10.1016/S1003-6326(21)65730-8.

[5] H. Köçkar, N. Kaplan, Single crystal martensitic phase of structural properties-related magnetic behaviour of FeCrNi thin films: in-plane magnetic anisotropy under different substrate rotation speeds, J. Mater. Sci. Mater. Electron. 31 (2020) 12823–12829, https://doi.org/10.1007/s10854-020-03835-4.

[6] H. Köçkar, N. Kaplan, Investigation of soft magnetic properties of Ni/Cu multilayer films: definitive screening design and response surface methodology, J. Mater. Sci. Mater. Electron. 32 (2021) 20955–20964, https://doi.org/10.1007/s10854-021-06506-0.

[7] X. Xu, C. Zhang, H.A. Derazkola, M. Demiral, A.M. Zain, A. Khan, UFSW tool pin profile effects on properties of aluminium-steel joint, Vacuum 192 (2021), 110460, https://doi.org/10.1016/j.vacuum.2021.110460.

[8] P. Talebizadehsardari, F. Musharavati, A. Khan, T.A. Sebaey, A. Eyvaziana, H.A. Derazkola, Underwater friction stir welding of Al-Mg alloy: thermo-mechanical modeling and validation, Mater. Today Commun. 26 (2021), 101965, https://doi.org/10.1016/j.mtcomm.2020.101965.

[9] Y. Zhao, J. You, J. Qin, C. Dong, L. Liu, Z. Liu, S. Miao, Stationary shoulder friction stir welding of Al–Cu dissimilar materials and its mechanism for improving the microstructures and mechanical properties of joint, Mater. Sci. Eng. A 837 (2022), 142754, https://doi.org/10.1016/j.msea.2022.142754.

[10] Tiwan, M.N. Ilman, Kusmono Microstructure and mechanical properties of friction stir spot welded AA5052-H112 aluminum alloy, Heliyon 7 (2021), e06009, https://doi.org/10.1016/j.heliyon.2021.e06009.

[11] M. Li, C. Zhang, D. Wang, L. Zhou, D. Wellmann, Y. Tian, Friction stir spot welding of aluminum and copper: a review, Materials 13 (2020) 156.

[12] K. Mehta, A. Astarita, P. Carlone, R. Della Gatta, H. Vyas, P. Vilaça, F. Tucci, Investigation of exit-hole repairing on dissimilar aluminum-copper friction stir welded joints, J. Mater. Res. Technol. 13 (2021) 2180–2193, https://doi.org/10.1016/j.jmrt.2021.06.019.

[13] X.W. Li, D.T. Zhang, C. Qiu, W. Zhang, Microstructure and mechanical properties of dissimilar pure copper/1350 aluminum alloy butt joints by friction stir welding, Trans. Nonferrous Met. Soc. China (English Ed. 22 (2012) 1298–1306, https://doi.org/10.1016/S1003-6326(11)61318-6.

[14] S. Shankar, S. Chattopadhyaya, Friction stir welding of commercially pure copper and 1050 aluminum alloys, Mater. Today Proc. 25 (2019) 664–667, https://doi.org/10.1016/j.matpr.2019.07.719.

[15] P. Liu, Q. Shi, W. Wang, X. Wang, Z. Zhang, Microstructure and XRD analysis of FSW joints for copper T2/aluminium 5A06 dissimilar materials, Mater. Lett. 62 (2008) 4106–4108, https://doi.org/10.1016/j.matlet.2008.06.004.

[16] I. Galvão, A. Loureiro, D. Verdera, D. Gesto, D.M. Rodrigues, Influence of tool offsetting on the structure and morphology of dissimilar aluminum to copper friction-stir welds, Metall. Mater. Trans. A Phys. Metall. Mater. Sci. 43 (2012) 5096–5105, https://doi.org/10.1007/s11661-012-1351-x.

[17] I. Galvao, D. Verdera, D. Gesto, A. Loureiro, D.M. Rodrigues, Analysing the challenge of aluminium to copper FSW, in: Proceedings of the 9th International Symposium on Friction Stir Welding, 2012, pp. 891–907.

[18] P. Xue, B.L. Xiao, D. Wang, Z.Y. Ma, Achieving high property friction stir welded aluminium/copper lap joint at low heat input, Sci. Technol. Weld. Join. 16 (2011) 657–661, https://doi.org/10.1179/1362171811Y.0000000018.

[19] T. Saeid, A. Abdollah-zadeh, B. Sazgari, Weldability and mechanical properties of dissimilar aluminum-copper lap joints made by friction stir welding, J. Alloys Compd. 490 (2010) 652–655, https://doi.org/10.1016/j.jallcom.2009.10.127.

[20] C.W. Tan, Z.G. Jiang, L.Q. Li, Y.B. Chen, X.Y. Chen, Microstructural evolution and mechanical properties of dissimilar Al-Cu joints produced by friction stir welding, Mater. Des. 51 (2013) 466–473, https://doi.org/10.1016/j.matdes.2013.04.056.

[21] P. Xue, B.L. Xiao, D.R. Ni, Z.Y. Ma, Enhanced mechanical properties of friction stir welded dissimilar Al-Cu joint by intermetallic compounds, Mater. Sci. Eng. A 527 (2010) 5723–5727, https://doi.org/10.1016/j.msea.2010.05.061.

[22] P. Xue, D.R. Ni, D. Wang, B.L. Xiao, Z.Y. Ma, Effect of friction stir welding parameters on the microstructure and mechanical properties of the dissimilar Al-Cu joints, Mater. Sci. Eng. A 528 (2011) 4683–4689, https://doi.org/10.1016/j.msea.2011.02.067.

[23] M.E. Aalami-Aleagha, B. Hadi, M.A. Shahbazi, 3-Dimensional numerical analysis of friction stir welding of copper and aluminum, J. Mech. Sci. Technol. 30 (2016) 3767–3776, https://doi.org/10.1007/s12206-016-0739-8.
[24] H. Sun, Q. Zhou, J. Zhu, Y. Peng, X. Ma, Analysis of the temperature field in Al-Cu dissimilar materials friction stir welding, J. Mater. Eng. Perform. 28 (2019) 3115–3128, https://doi.org/10.1007/s11665-019-04024-z.
[25] A.K. Kadian, P. Biswas, The study of material flow behaviour in dissimilar material FSW of AA6061 and Cu-B370 alloys plates, J. Manuf. Process. 34 (2018) 96–105, https://doi.org/10.1016/j.jmapro.2018.05.035.
[26] M. Iordache, E. Nitu, C. Badulescu, D. Iacomi, L.N. Boţilă, B. Radu, Evaluation of thermal distribution in friction stir welding on dissimilar materials (Cu-Al) using infrared thermography and numerical simulation, Adv. Mater. Res. 1138 (2016) 113–118, https://doi.org/10.4028/www.scientific.net/amr.1138.113.
[27] N.P. Patel, P. Parlikar, R. Singh Dhari, K. Mehta, M. Pandya, Numerical modelling on cooling assisted friction stir welding of dissimilar Al-Cu joint, J. Manuf. Process. 47 (2019) 98–109, https://doi.org/10.1016/j.jmapro.2019.09.020.
[28] M. Fallahati Naqibi, M. Elyasi, H. Jamshidi Aval, M.J. Mirnia, Investigation of friction-stir welding parameters in the fabrication of a 2-layer aluminum–copper pipe with monolithic interface, Trans. Indian Inst. Met. 74 (2021) 285–300, https://doi.org/10.1007/s12666-020-02127-z.
[29] M.S.M. Isa, K. Moghadasi, M.A. Ariffin, S. Raja, M.R. bin Muhamad, F. Yusof, M.F. Jamaludin, N. bin Yusoff, Ab Karim, M.S. bin, Recent research progress in friction stir welding of aluminium and copper dissimilar joint: a review, J. Mater. Res. Technol. 15 (2021) 2735–2780, https://doi.org/10.1016/j.jmrt.2021.09.037.
[30] H. Aghajani Derazkola, A. Eyvazian, A. Simchi, Submerged friction stir welding of dissimilar joints between an Al-Mg alloy and low carbon steel: thermo-mechanical modeling, microstructural features, and mechanical properties, J. Manuf. Process. 50 (2020) 68–79, https://doi.org/10.1016/j.jmapro.2019.12.035.
[31] X. Liu, G. Chen, J. Ni, Z. Feng, Computational fluid dynamics modeling on steady-state friction stir welding of aluminum alloy 6061 to TRIP steel, J. Manuf. Sci. Eng. Trans. ASME 139 (2017), https://doi.org/10.1115/1.4034895.
[32] X. Liu, S. Lan, J. Ni, Thermal mechanical modeling of the plunge stage during friction-stir welding of dissimilar Al 6061 to TRIP 780 steel, J. Manuf. Sci. Eng. Trans. ASME 137 (2015), https://doi.org/10.1115/1.4031188.
[33] D.O. Bokov, M.A. Jawad, W. Suksatan, M.E. Abdullah, A. Świerczyńska, D. Fydrych, H.A. Derazkola, Effect of pin shape on thermal history of aluminum-steel friction stir welded joint: computational fluid dynamic modeling and validation, Materials (2021) 14.
[34] H. Aghajani Derazkola, N. Kordani, H. Aghajani Derazkola, Effects of friction stir welding tool tilt angle on properties of Al-Mg-Si alloy T-joint, CIRP J. Manuf. Sci. Technol. 33 (2021) 264–276, https://doi.org/10.1016/j.cirpj.2021.03.015.
[35] S. Memon, D. Fydrych, A.C. Fernandez, H.A. Derazkola, H.A. Derazkola, Effects of fsw tool plunge depth on properties of an al-mg-si alloy t-joint: thermomechanical modeling and experimental evaluation, Materials (2021) 14.
[36] H. Aghajani Derazkola, E. Garcia, M. Elyasi, Underwater friction stir welding of PC: experimental study and thermo-mechanical modelling, J. Manuf. Process. 65 (2021) 161–173, https://doi.org/10.1016/j.jmapro.2021.03.034.
[37] H.I. Khalaf, R. Al-sabur, M.E. Abdullah, A. Kubit, H.A. Derazkola, Effects of underwater friction stir welding heat generation on residual stress of AA6068-T6 aluminum alloy, Materials 15 (2022).
[38] A. Eyvazian, A. Hamouda, F. Tarlochan, H.A. Derazkola, F. Khodabakhshi, Simulation and experimental study of underwater dissimilar friction-stir welding between aluminium and steel, J. Mater. Res. Technol. 9 (2020) 3767–3781, https://doi.org/10.1016/j.jmrt.2020.02.003.